FORWARD-IN-TIME DIFFERENCING FOR FLUIDS: NONHYDROSTATIC MODELING OF FLUID MOTIONS ON A SPHERE

Piotr K Smolarkiewicz*, Vanda Grubišić*, Len G Margolin†
and Andrzej A Wyszogrodzki§*
*National Center for Atmospheric Research, Boulder, Colorado, U.S.A.
† Los Alamos National Laboratory, Los Alamos, New Mexico, U.S.A.
§University of Warsaw, Warsaw, Poland

1. INTRODUCTION

Traditionally, numerical models for simulating planetary scale weather and climate employ the hydrostatic primitive equations—an abbreviated form of Navier-Stokes' equations that neglect vertical accelerations and use simplified Coriolis forces.[1] Although there is no evidence so far that including nonhydrostatic effects in global models has any physical significance for large scale solutions, there is an emerging trend in the community toward restoring Navier-Stokes' equations (or at least their less constrained forms) in global models of atmospheres and oceans (Cullen et al.1997, Marshall et al.1997a, Semazzi et al.1995). The primary motivation is that state-of-the-art computers already admit resolutions where local nonhydrostatic effects become noticeable. Other advantages include: the convenience of local mesh refinement; better overall accuracy; insubstantial computational overhead relative to hydrostatic models; universality and therefore convenience of maintaining a single large code; conceptual simplicity and mathematical elegance—features important for education.

The few existing nonhydrostatic global models differ in analytic formulation and numerical design, reflecting their different origins and purposes. Much of our present research (Anderson et al.1997; Smolarkiewicz and Margolin 1997) aims to improve the design of a high-performance numerical model for simulating the flows of moist (and precipitating), rotating, stratified fluids past a specified time-dependent irregular lower boundary. This model is representative of a class of nonhydrostatic atmospheric codes that employs the anelastic equations of motion in a terrain-following curvilinear framework, and contains parallel implementations of semi-Lagrangian and Eulerian approximations (Smolarkiewicz and Pudykiewicz 1992, Smolarkiewicz and Margolin 1993) selectable by the user. The model has been employed in a variety of applications; the quality of results suggest that modern nonoscillatory forward-in-time (NFT) methods are superior to the more traditional centered-in-time-and-space schemes, in terms of accuracy, computational efficiency, flexibility and robustness

[1]For a thorough critique of the hydrostatic primitive equations see Marshall et al. 1997b.

(Smolarkiewicz and Margolin 1997, 1998).

We have extended the Cartesian NFT model to a mountaineous sphere and, consequently, have dispensed with the traditional geophysical simplifications of hydrostaticity, gentle terrain slopes, and weak rotation. In this paper, we discuss the algorithmic design, relative efficiency and accuracy of several different variants (hydrostatic, nonhydrostatic, implicit, explicit, etc.) of the NFT global model. We substantiate our theoretical discussions with the results of simulations of idealized global orographic flows and climates.

2. MODEL DESCRIPTION

The small-scale numerical model used as the basis of the global model discussed in this study has been described in Smolarkiewicz and Margolin (1997). It is representative of a class of nonhydrostatic atmospheric models that solve the anelastic equations of motion in standard, nonorthogonal terrain-following coordinates. The extended global model results from a composition of two mappings: it can be derived by either transforming the small-scale model equations to spherical coordinates, or by transforming the anelastic variant of the Navier-Stokes' equations on a rotating sphere (cf. section 4.12 in Gill 1982) to terrain-following coordinates. Below we comment briefly on the essential aspects of the design of the extended global model while referring the reader to earlier work for further details.

2.1 Analytic formulation

In this paper, we focus on an inviscid, adiabatic, density-stratified fluid whose undisturbed, geostrophically-balanced "ambient" state is described by the potential temperature $\Theta_e = \Theta_e(\mathbf{x})$ and the velocity $\mathbf{v}_e = \mathbf{v}_e(\mathbf{x})$. The nonorthogonal terrain-following system of coordinates $[x,\ y,\ z] = [R\lambda,\ R\phi,\ H(r-h)/(H-h)]$ assumes a model depth H and an irregular (but at least twice-differentiable) lower boundary $h = h(x,\ y)$. Here r, R, λ, and ϕ denote, respectively, the radial component of the vector radius, sphere's radius, longitude, and latitude. The coordinate transformation enters the governing equations of motion through the coefficients of the metric tensor $G^{IJ} = (\partial x^I/\partial x_C^K)(\partial x^J/\partial x_C^K)$, and the Jacobian of transformation $G = Det\{\partial \mathbf{x}_C/\partial \mathbf{x}\} = (Det\{G^{IJ}\})^{-1/2}$, where the subscript C refers to Cartesian coordinates. In particular, $G^{11} = (\Gamma\cos\phi)^{-1}$, $G^{13} = G^{11}G_o^{13}$, $G^{22} = \Gamma^{-1}$, $G^{23} = G^{22}G_o^{23}$, and $G = G_o\Gamma^2\cos\phi$. Here, $\Gamma \equiv r/R$, and the subscript o refers to the metric coefficients of the standard terrain-following transformation from a Cartesian space (Gal-Chen and Somerville 1975). The remaining coefficients are as in the standard transformation.

Given the assumptions above, the governing anelastic equations may be written compactly as follows:

$$\frac{Du}{Dt} = -G^{11}\frac{\partial \pi}{\partial x} - G^{13}\frac{\partial \pi}{\partial z} + fv' - \hat{f}w' - \alpha u' + \frac{(uv)'}{\Gamma R}\mathrm{tg}\phi - \frac{(uw)'}{\Gamma R} \equiv F^u\ , \qquad (1a)$$

$$\frac{Dv}{Dt} = -G^{22}\frac{\partial \pi}{\partial y} - G^{23}\frac{\partial \pi}{\partial z} - fu' - \alpha v' - \frac{(uu)'}{\Gamma R}\mathrm{tg}\phi - \frac{(vw)'}{\Gamma R} \equiv F^v \ , \tag{1b}$$

$$\frac{Dw}{Dt} = -G_o^{-1}\frac{\partial \pi}{\partial z} + g\frac{\Theta'}{\overline{\Theta}} + \hat{f}u' - \alpha w' + \frac{(u^2+v^2)'}{\Gamma R} \equiv F^w \ , \tag{1c}$$

$$\frac{D\Theta}{Dt} = -\tilde{\alpha}\Theta' \equiv F^\Theta \ , \tag{1d}$$

$$\frac{\partial \overline{\rho} G G^{11} u}{\partial x} + \frac{\partial \overline{\rho} G G^{22} v}{\partial y} + \frac{\partial \overline{\rho} G \omega}{\partial z} = 0 \ . \tag{1e}$$

Here π is the pressure perturbation with respect to the ambient state normalized by the anelastic density. Θ is the potential temperature, $f = 2\Omega \sin\phi$ and $\hat{f} = 2\Omega\cos\phi$ are the radial and latitudinal components of the planetary rotation vector $\mathbf{\Omega}$, g is the acceleration due to gravity, and $\omega \equiv \dot{z}$ is the "vertical" component of the transformed (contravariant) velocity, related to the covariant velocity components of a local tangent Cartesian framework (aligned with standard geographical coordinates) through

$$\omega = G_o^{-1} w + G^{13} u + G^{23} v \ , \tag{2}$$

and $\dot{x} = G^{11}u$, and $\dot{y} = G^{22}v$. The potential temperature $\overline{\Theta} = \overline{\Theta}(r')$, $r' \equiv r - R$, which appears in the denominator of the buoyancy term in (1c), and the anelastic density $\overline{\rho} = \overline{\rho}(r')$ in the mass continuity equation (1e) refer to the hydrostatic reference state of the Boussinesq expansion around a constant stability profile. The attenuation forcings that appear in the momentum and entropy equations (1a)-(1d) simulate wave-absorbing devices employed typically in the vicinity of the open upper boundary of the problem domain, and primes denote deviations from ambient values.

Mathematically, the formulation in (1)-(2) is analogous to that of the small-scale model except for the metric forces in (1a)-(1c) proportional to products of various velocity components (cf. Clark et al.1996). Similarly, the finite-difference approximations employed to solve (1) closely follow the approach adopted in the small-scale model.

2.2 Finite-difference approximations

2.2.1 *Basic model algorithm*

Our basic algorithm for integrating (1) on a discrete mesh is second-order-accurate in space and time. Time marching is based on two-time-level NFT transport methods. In general, there are two options for the spatial differencing—semi-Lagrangian (Smolarkiewicz and Pudykiewicz 1992) and Eulerian (Smolarkiewicz and Margolin 1993). The lattice structure assumes all prognostic variables defined at the same grid points $\mathbf{x_i}$—important for the efficacy of the unified semi-Lagrangian/Eulerian NFT approach (Smolarkiewicz and Margolin 1997).

We write the finite-difference approximations to the prognostic equations (1a)-(1d) in the compact

form

$$\psi_{\mathbf{i}}^{n+1} = LE(\widetilde{\psi}) + 0.5\Delta t \mathbf{F}_{\mathbf{i}}^{n+1} \ . \tag{3}$$

Here, LE denotes either an advective semi-Lagrangian or a flux-form Eulerian NFT transport operator (sections 3.1 and 3.2 in Smolarkiewicz and Margolin 1997, respectively);[2] $\widetilde{\psi} \equiv \psi^n + 0.5\Delta t \mathbf{F}^n$, where ψ and $\mathbf{F}$ denote vectors of the dependent variables u, v, w, and Θ and the associated forcings appearing in (1); and the indices $\mathbf{i}$ and n denote the spatial and temporal location on a (*logically*) rectangular Cartesian mesh. Completion of the model algorithm requires a straightforward algebraic inversion of the system (3), which is implicit with respect to Θ, u, v, and w; and the formulation of the boundary value problem for pressure π implied by the continuity constraint (1e). [Some details of the formulation as well as the explicit form of the resulting operator for the implicit variant of the model, introduced later in section 2.2.4, can be found in Appendix B.] The resulting elliptic equation is solved (subject to appropriate boundary conditions; section 4b in Smolarkiewicz and Margolin 1994) using the generalized conjugate-residual (GCR) approach (Eisenstat et al.1983, Smolarkiewicz et al.1997) summarized in Appendix A.

2.2.2 *Metric forces*

In order to avoid solving a nonlinear elliptic equation for pressure, the metric forces contributing to $\mathbf{F}^{n+1}$ on the RHS of (3) are either approximated explicitly (e.g., in the spirit of Adams-Bashfort schemes), or the entire subset of (3) corresponding to the momentum equations (1a)-(1c) is iterated with the metric terms lagged behind. In both cases the metric forces enter the RHS of the resulting *linear* elliptic pressure equation. Although the iterative approach requires solving the elliptic equation at each iteration, it is overall advantageous: In the limit, it converges to the trapezoidal-rule approximation, which preserves the neutral character of the metric force. With the first guess $\mathbf{F}^{n+1}|^0 = \mathbf{F}^n$, one iteration suffices for second-order accuracy. In typical applications for flows on the Earth, the results are insensitive to the number of iterations beyond 2, and the overhead associated with two passes through the pressure solver is insignificant, as the second pass requires merely a few iterations of the GCR solver to maintain the accuracy of the first pass.

2.2.3 *Pressure solver*

Because NFT methods are inherently two-time-level, an accurate (time-centered) integration of forces leads to the inversion of a large nonsymmetric linear system that represents a complex nonself-adjoint 3D elliptic PDE for pressure. For atmospheres whose depth is comparable to the radius of the

[2]Specifically, the semi-Lagrangian algorithm remaps transported fields to the departure points of flow trajectories arriving at grid points $(\mathbf{x}_\mathbf{i},\ t^{n+1})$ (Smolarkiewicz and Grell 1992), while the Eulerian scheme integrates the homogeneous transport equation $\overline{\rho}\widetilde{\psi},t + \nabla \cdot (\overline{\rho}\mathbf{V}\widetilde{\psi}) = 0$, where $\mathbf{V} \equiv (G^{11}u,\ G^{22}v,\ \omega)$ (Smolarkiewicz and Clark 1986).

sphere, such a problem can be solved easily using standard Krylov subspace methods for nonsymmetric operators (Smolarkiewicz and Margolin 1994, Smolarkiewicz et al.1997). For thin atmospheres typical of Earth meteorology, however, the resulting elliptic operator is extremely stiff [3], necessitating additional enhancements to the Krylov solvers to assure their convergence as well as to reduce the number of iterations. We have explored two (not necessarily exclusive) strategies. One is to use the hydrostatic solution for pressure as an initial guess for the (iterative) nonhydrostatic pressure solver. This procedure naturally facilitates the optional implementation of hydrostatic or nonhydrostatic models, leaving the final choice to the user. The second strategy uses ADI-type preconditioners (Skamarock et al.1997) for the Krylov solver, and dispenses with the decomposition of the pressure into a hydrostatic and a nonhydrostatic part (Marshall et al.1997a). This results in a simpler, more general, and elegant variant of the model.

A particularly simple and effective preconditioner used in the stage $(A3e)$ of the GCR procedure (Appendix A) derives from the implicit stationary Richardson iteration

$$\frac{q_{\mathbf{i}}^{\mu+1} - q_{\mathbf{i}}^{\mu}}{\Delta\widetilde{\tau}} = \mathcal{P}_{\mathbf{i}}^{h}(q^{\mu}) + \mathcal{P}_{\mathbf{i}}^{z}(q^{\mu+1}) - r_{\mathbf{i}}^{\nu+1} \ , \tag{4}$$

where q denotes an error estimate between the current iterate of π and the exact solution, r is the residual error, $\mathcal{P}$ is an abbreviated form of $\mathcal{L}$ in $(A3f)$ with all "off-diagonal" coefficients C^{IJ} set to zero, $\mathcal{P}^h$ and $\mathcal{P}^z$ are the horizontal and the vertical counterparts of the operator $\mathcal{P}$, respectively, $\Delta\widetilde{\tau}$ is a parameter of the iteration (a pseudo-time step) based on spectral properties of $\mathcal{P}^h$ [*viz.*, linear stability analysis of (4)], μ numbers successive Richardson iterations, and ν numbers the outer iterations of the GCR solver. The equation (4) leads to a linear problem

$$(\mathcal{I} - \Delta\widetilde{\tau}\mathcal{P}^z)q^{\mu+1} = \widetilde{R}^{\mu} \ , \tag{5}$$

where $\forall_{\mathbf{i}} \ \widetilde{R}_{\mathbf{i}}^{\mu} \equiv q_{\mathbf{i}}^{\mu} + \Delta\widetilde{\tau}(\mathcal{P}_{\mathbf{i}}^{h}(q^{\mu}) - r_{\mathbf{i}}^{\nu+1})$, that can be solved readily using the celebrated tridiagonal algorithm (cf. Appendix A in Roache 1972).[4] The majority of results shown in this paper use the fourth-order GCR [i.e., GCR(k) with $k = 4$ in Appendix A] with eight inner iterations in (4).

In a series of numerical experiments for continuously stratified flows past a large isolated mountain in mid latitudes (discussed later in section 3.1 of this paper), we have verified that both hydrostatic and nonhydrostatic models reproduce the same solution. The solution differences take the form of horizontally propagating inertia-gravity waves (cf. Fig. 2b in section 3.1) with a maximal vertical velocity $\sim 10^{-3}$ ms^{-1} that is an order of magnitude less than the vertical velocities of the actual flow. The relative overhead of solving the nonhydrostatic problem is $\sim 80\%$ in the model where

[3] A reasonable estimate of the spectral condition number is $\kappa \sim \mathcal{O}(10^{10})$.

[4] On the nonstaggered mesh used here, the resulting liner problem is formally pentadiagonal and requires a customized tridiagonal algorithm for its inversion.

the nonhydrostatic solution is sought as a perturbation to the hydrostatic result, but only $\sim 40\%$ in the simpler model without the hydrostatic counterpart. We believe the latter number can be reduced substantially by accelerating the elliptic solver with improved preconditioners. In light of these results, pursuit of the hydrostatic approach seems unjustified.

2.2.4 *Implicit variant*

In the basic version of the model, the entropy equation (1d) is integrated prior to the momentum equations. This allows the buoyancy term in (1c) to be evaluated explicitly at $n+1$ in (3)—in the spirit of Runge-Kutta schemes—and to enter the RHS of the elliptic pressure equation. Consequently, the numerical stability of the basic model depends primarily on the propagation speed of internal gravity waves.[5] Another implicit variant of the model replaces (1d) with

$$\frac{D\Theta'}{Dt} = -G^{11}u\frac{\partial\Theta_e}{\partial x} - G^{22}v\frac{\partial\Theta_e}{\partial y} - \omega\frac{\partial\Theta_e}{\partial z} - \tilde{\alpha}\Theta' \ , \tag{6}$$

solved simultaneously with the momentum equations; the buoyancy term in (1c) is evaluated implicitly at $n+1$ in (3)—in the spirit of the trapezoidal-rule scheme—and enters both the RHS and the coefficients of the elliptic pressure equation (see Appendix B for details). The numerical stability of this variant of the model is controlled solely by proper limiting of Courant and Lipschitz numbers $\mathrm{C} = \| \Delta t\mathbf{V}/\Delta\mathbf{X} \|$ and $\mathrm{L} = \| \Delta t(\partial\mathbf{V}/\partial\mathbf{x}) \|$, respectively, for the Eulerian and semi-Lagrangian options of the solver. For smooth flows, the latter option admits large time steps characteristic of semi-implicit semi-Lagrangian models.

3. EXAMPLES

3.1 Orographic flow

Figure 1 shows the pattern of vertical and meridional velocity components after 15 days of simulated zonal flow of a stratified Boussinesq fluid past a large hill (cf. Grose and Hoskins 1979, Williamson et al.1992) using the semi-Lagrangian implicit variant of the model discussed above. The flow parameters are:

$$u_e = \hat{U}(r')\cos\phi \ , \quad v_e = 0 \ , \quad \hat{U}(r') = U_o\Gamma \ , \quad U_o = 20 \ \mathrm{ms}^{-1} \ ; \tag{7}$$

the corresponding thermally-balanced

$$\Theta_e = \hat{\Theta}_e(r') + \frac{\overline{\Theta}}{g}\sin^2\phi\left[\frac{\hat{U}^2}{\Gamma R} + f_o\hat{U} - \frac{1}{2}\frac{\partial}{\partial r}\left(\hat{U}^2 + \hat{U}\Gamma f_o R\right)\right] \ , \tag{8}$$

where $\hat{\Theta}_e(r') = \Theta_o[1 + r'N^2/g]$ and the Brunt-Väisällä frequency $N = 10^{-2}$ s^{-1}. The conical hill with height $2 \cdot 10^3$ m and angular base radius $\Pi/9$ is centered at $(\lambda, \ \phi) = (3/2\Pi, \ 1/6\Pi)$. The globe is

[5] External gravity modes are eliminated by assuming a rigid-lid upper boundary.

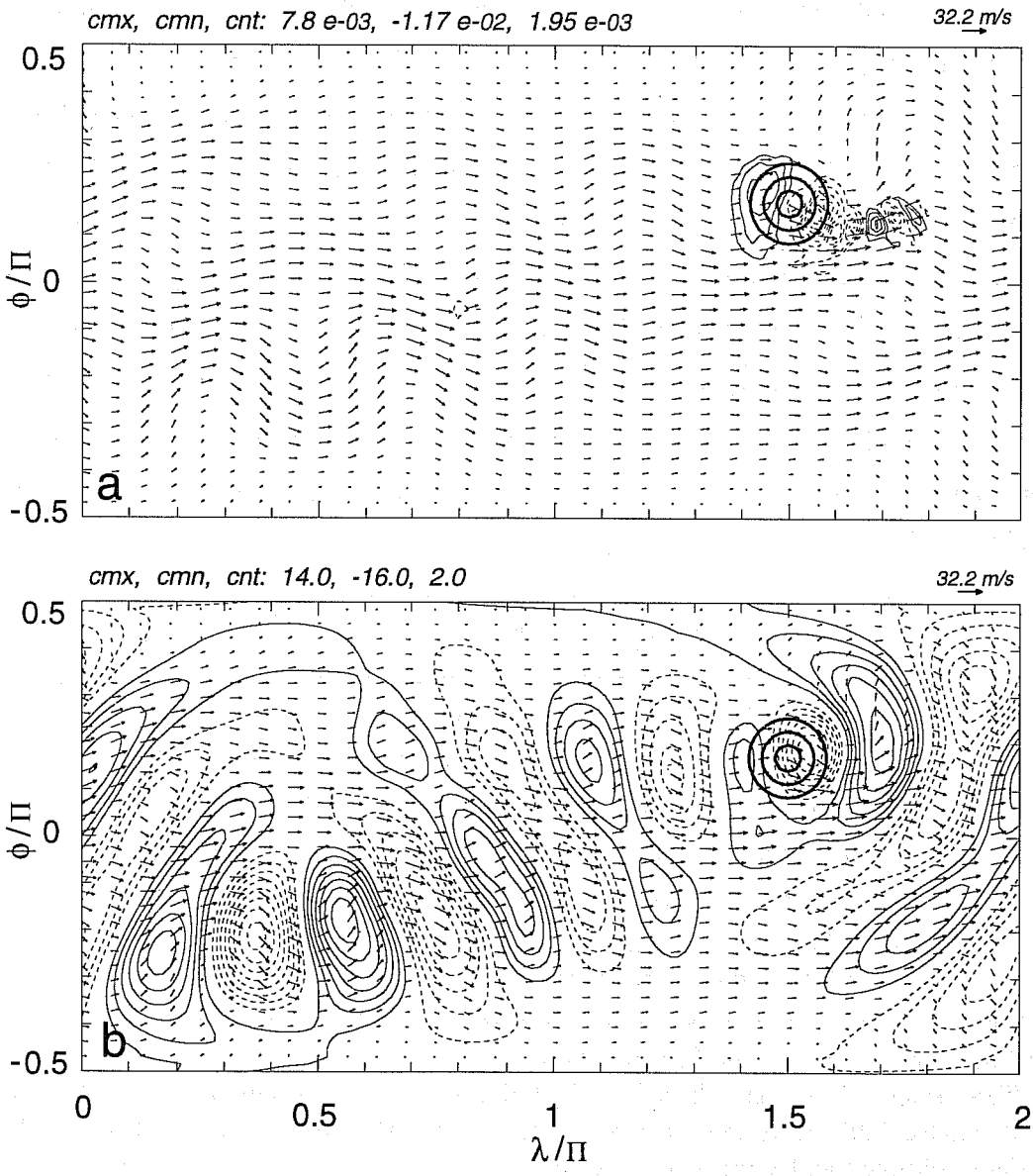

Figure 1: Planetary wave propagation on a sphere. Contours show patterns of vertical and meridional velocity components in ms^{-1} (plates a and b, respectively) at 4 km after 15 days of simulation. Contour extrema and intervals are shown in the upper left corner of each plate. Negative values are dashed, and zero contours are omitted. The mountain is illustrated with thick solid circles. Maximum vector lengths (here identical) are shown in the upper right corner of each plate.

covered with a uniform spherical mesh with $nx \times ny = 128 \times 64$ grid intervals (no grid points at the poles) and the $H = 8 \cdot 10^3$ m deep atmosphere is resolved with $nz = 20$ uniform grid intervals. The time step of integration is $\Delta t = 7.2 \cdot 10^3$ s.

The simulation in Fig. 1 employs no viscous filters, and the only dissipation is that due to the monotonicity constraints built into the remapping algorithm (Smolarkiewicz and Grell 1992). The execution time on a single processor CRAY J-90 is $\sim 1.4 \cdot 10^4$ s. This value can be easily reduced by a factor of about 2 by using dissipative filters in polar regions (a common practice in global circulation models). At the large time step employed here, most of the computational effort is already in the elliptic solver, so that overall model efficiency strongly depends on such technical issues as stopping criteria (Smolarkiewicz et al.1997) and effective preconditioning (Skamarock et al.1997). We believe that further improvement in the latter will lead to substantial acceleration of the model.

In order to establish the solution dependence on model design and on the numerical scheme employed, as well as on alternate formulations of the governing equations of motion, we have performed a series of simulations like that in Fig. 1. The results of this sensitivity study are summarized in Tables 1 to 5.

Run	Solver-Δt	$\| v \|_\infty$	$\| v \|_2$	$\| w \|_\infty$	$\| w \|_2$	CPU
1	EU-2400	20.6	5.0	$2.3 \cdot 10^{-2}$	$9.6 \cdot 10^{-4}$	291
2	SL-2400	20.5	4.8	$2.2 \cdot 10^{-2}$	$9.4 \cdot 10^{-4}$	378
3	SL-7200	20.6	4.8	$2.2 \cdot 10^{-2}$	$9.6 \cdot 10^{-4}$	226
3b	SL-7200$^\epsilon$	21.0	4.8	$2.2 \cdot 10^{-2}$	$9.4 \cdot 10^{-4}$	616
4	SL-1200	20.7	4.8	$2.2 \cdot 10^{-2}$	$9.3 \cdot 10^{-4}$	527
5	EU-1200	20.9	5.1	$2.3 \cdot 10^{-2}$	$9.7 \cdot 10^{-4}$	377

Table 1: Comparison of various executions of the semi-implicit anelastic model for simulating the 15-day evolution of the orographic flow on the sphere. The first column numbers runs, for further reference. The second column lists the solver (Eulerian vs. semi-Lagrangian) and the time step (Δt in s) employed; run SL-7200$^\epsilon$ tests the convergence criterion in the pressure solver. Columns 3-6 provide norms of the meridional and vertical velocity components (in ms^{-1}), respectively. The last column lists single-processor Cray J90 CPU times (min).

Tables 1 to 4 collect various runs in a certain logical order. Table 1 contains semi-Lagrangian and Eulerian runs of the semi-implicit model (section 2.2.4) at different time steps; run 3b is identical to run 3 except for the order of magnitude tighter convergence criterion in the GCR pressure solver. Table 2 contains hydrostatic and nonhydrostatic runs using explicit (with respect to internal gravity waves) variants of the model (section 2.2.1). Since the explicit model runs are unreasonably expensive, further applications of the explicit models (Tables 3 and 4) incorporate a heavy dissipative filter in

polar regions [in (1a)-(1d), $\alpha = \tilde{\alpha}$ increases linearly from 0 to 1/150 s^{-1} over the five grid intervals near each pole] to allow for a substantially larger time step. Thus, runs 9 and 10 in Table 3 were designed to make runs 8 (Table 2) and 4 (Table 1) directly comparable. Finally, Table 4 collects results of the simulations using alternate governing equations of motion (1a)-(1e).

Run	Solver-Δt	$\| v \|_\infty$	$\| v \|_2$	$\| w \|_\infty$	$\| w \|_2$	CPU
6	HNH-h	21.7	4.6	$2.1 \cdot 10^{-2}$	$8.8 \cdot 10^{-4}$	1328
7	HNH-nh	21.9	4.6	$2.1 \cdot 10^{-2}$	$8.8 \cdot 10^{-4}$	2407
8	ADIprc	21.0	4.6	$2.1 \cdot 10^{-2}$	$8.9 \cdot 10^{-4}$	1900

Table 2: As in Table 1 but for three different explicit semi-Lagrangian anelastic models. Runs 6 and 7 are for the hydrostatic and nonhydrostatic options of the model based on the hydrostatic first guess, and run 8 is for the alternate nonhydrostatic model with an ADI-type preconditioner of the 3D elliptic pressure solver; $\Delta t = 150$ s.

Run	Solver-Δt	$\| v \|_\infty$	$\| v \|_2$	$\| w \|_\infty$	$\| w \|_2$	CPU
9	EXPL	20.3	4.6	$2.1 \cdot 10^{-2}$	$8.9 \cdot 10^{-4}$	704
10	IMPL	20.3	4.6	$2.1 \cdot 10^{-2}$	$8.9 \cdot 10^{-4}$	437

Table 3: As in Table 1 but for the explicit and semi-implicit nonhydrostatic semi-Lagrangian anelastic models; $\Delta t = 1200$ s with a heavy dissipative filter near the poles.

Run	Solver-Δt	$\| v \|_\infty$	$\| v \|_2$	$\| w \|_\infty$	$\| w \|_2$	CPU
11	INCM	19.7	4.6	$2.1 \cdot 10^{-2}$	$9.0 \cdot 10^{-4}$	677
12	ELAS	20.1	4.6	$2.1 \cdot 10^{-2}$	$9.0 \cdot 10^{-4}$	356

Table 4: As in Table 1 but for the incompressible Euler and elastic Boussinesq governing equations, simulated using explicit nonhydrostatic semi-Lagrangian models; $\Delta t = 1200$ s with the heavy filter near poles.

Run INCM in Table 4 uses the fully nonlinear incompressible Euler equations, and so addresses the impact of the Boussinesq approximation inherent in the anelastic model (1a)-(1e). The conversion from the anelastic to incompressible equations is achieved easily within the framework of the explicit numerical model (section 2.2.1). In detail (cf. Rotunno and Smolarkiewicz 1995), the conversion: i) replaces the pressure gradient terms $\partial\pi/\partial x_i$ with $\Theta^{-1}\partial\pi/\partial x_i$ terms, and the buoyancy term $g\Theta'/\overline{\Theta}$ with $-g\Theta'/\Theta$ term; ii) removes dependence on $\overline{\rho}$ from (1e); and iii) exploits Θ field for the fluid density $\rho(\mathbf{x}, t)$. Run ELAS, in turn, addresses the impact of incompressibility inherent in the anelastic model by admitting a finite speed of sound while retaining the Boussinesq approximation. This is a

Runs	$\| \delta v \|_\infty$	$\| \delta v \|_2$	$\| \delta w \|_\infty$	$\| \delta w \|_2$
$\Delta(3,4)$	3.3	0.79	$1.2 \cdot 10^{-2}$	$3.8 \cdot 10^{-4}$
$\Delta(3,2)$	2.8	0.66	$1.2 \cdot 10^{-2}$	$3.6 \cdot 10^{-4}$
$\Delta(3,3b)$	3.0	0.71	$2.3 \cdot 10^{-3}$	$8.9 \cdot 10^{-5}$
$\Delta(1,2)$	2.2	0.49	$6.8 \cdot 10^{-3}$	$2.6 \cdot 10^{-4}$
$\Delta(4,5)$	2.3	0.44	$6.4 \cdot 10^{-3}$	$2.6 \cdot 10^{-4}$
$\Delta(7,8)$	2.1	0.49	$2.3 \cdot 10^{-3}$	$1.7 \cdot 10^{-4}$
$\Delta(6,8)$	2.0	0.49	$2.2 \cdot 10^{-3}$	$1.7 \cdot 10^{-4}$
$\Delta(1,5)$	1.5	0.35	$4.1 \cdot 10^{-3}$	$1.6 \cdot 10^{-4}$
$\Delta(11,9)$	0.9	0.15	$2.1 \cdot 10^{-3}$	$1.5 \cdot 10^{-4}$
$\Delta(2,4)$	0.8	0.19	$2.0 \cdot 10^{-3}$	$8.7 \cdot 10^{-5}$
$\Delta(9,10)$	0.9	0.14	$2.3 \cdot 10^{-3}$	$7.7 \cdot 10^{-5}$
$\Delta(12,9)$	0.7	0.17	$6.6 \cdot 10^{-4}$	$6.1 \cdot 10^{-5}$
$\Delta(6,7)$	0.9	0.06	$7.9 \cdot 10^{-4}$	$7.9 \cdot 10^{-5}$

Table 5: Difference analysis of various runs collected in tables 1 to 4.

particularly simple alteration of the model (either explicit or implicit), merely replacing the anelastic mass continuity equation (1e) with

$$\frac{\partial \pi}{\partial t} + \frac{c_s^2}{\overline{\rho} G} \left(\frac{\partial \overline{\rho} G G^{11} u}{\partial x} + \frac{\partial \overline{\rho} G G^{22} v}{\partial y} + \frac{\partial \overline{\rho} G \omega}{\partial z} \right) = 0 \ , \tag{9}$$

where c_s is the speed of sound (taken here at 300 ms^{-1}). In effect, the Poisson equation for pressure (cf. Appendix B) is transformed into an appropriate, slightly better-conditioned Helmholtz equation.

All four tables list L_∞ and L_2 norms of the meridional and vertical velocity fields—natural perturbation fields with respect to the ambient flow (7)—as well as the computational expense of the model measured by the CPU time (in minutes). As evidenced by the values collected in tables, all the listed solutions agree to within about 10%. In fact, they are all similar to that shown in Fig. 1 and are hardly distinguishable in the figures. In order to quantify the differences between various experiments, we have performed analyses of the appropriate difference fields. The results are summarized in Table 5.[6]

Table 5 leads to a number of interesting conclusions. We draw attention to a few points that are especially noteworthy. The largest differences observed are due to the six-fold difference in Δt (using the semi-Lagrangian semi-implicit model from section 2.2.4), while the smallest differences are between the hydrostatic and nonhydrostatic model formulations. For illustration, in Fig. 2, we show the respective δw difference fields (cf. plate a in Fig. 1). The corresponding δv fields are not shown

[6]Our intention was to order the analyses of the difference fields in the decreasing magnitude of the differences. In some cases, this required a subjective judgement, since not all the norms used decrease at the same rate.

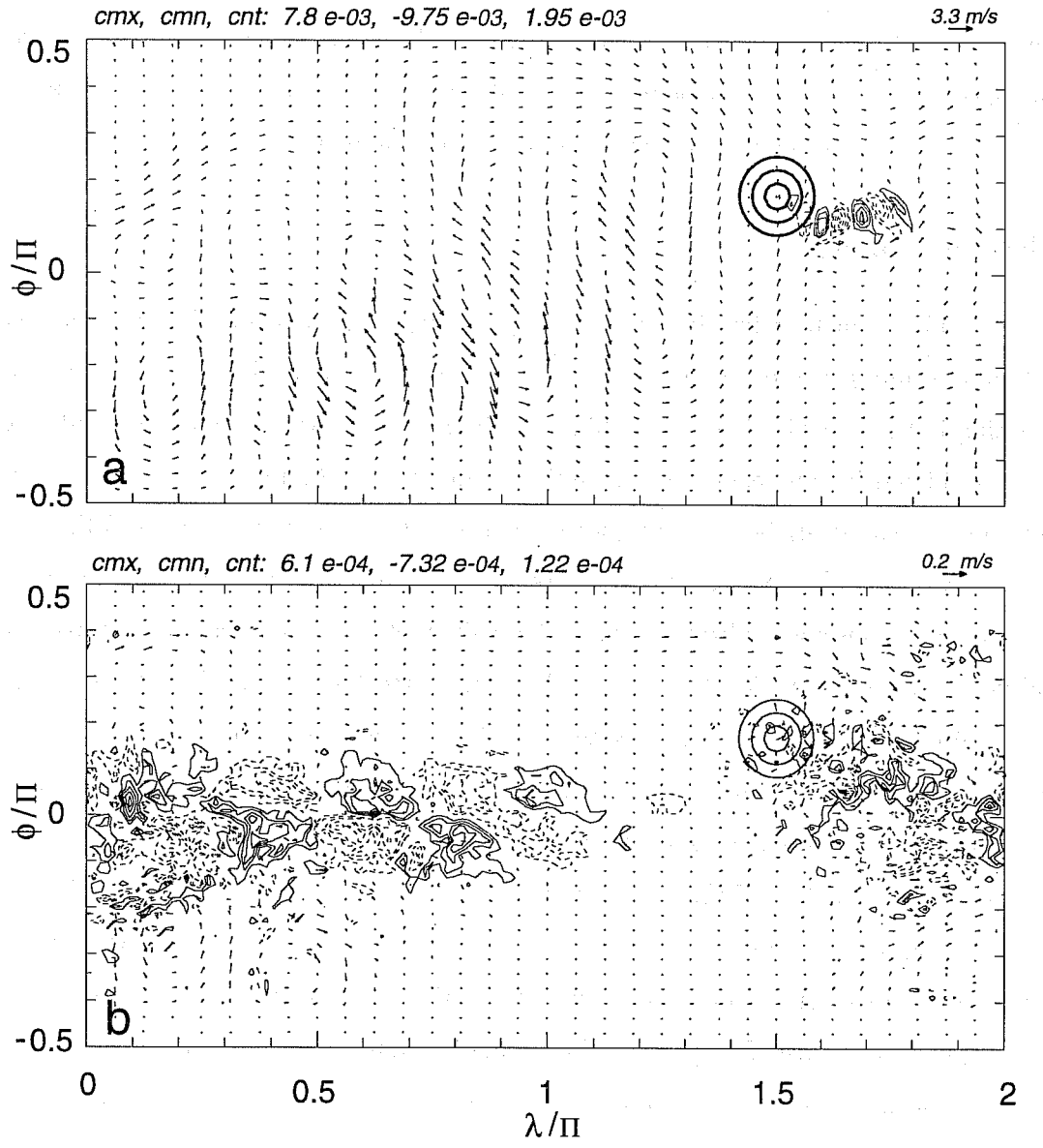

Figure 2: The vertical velocity difference field δw for the first $\Delta(3,4)$ and the last $\Delta(6,7)$ entry in Table 5 (plates a and b, respectively). The contouring convention is the same as in Fig. 1.

because: i) they mostly mimic the wave field in plate b of Fig. 1, so the numeric values of the δv norms in Table 5 adequately describe the differences; and ii) the vectors of the flow difference already give a sense of δv field. In general, "physical" differences [hydrostatic vs. nonhydrostatic $\Delta(6,7)$, elastic vs. anelastic $\Delta(12,9)$, incompressible Euler vs. Boussinesq $\Delta(11,9)$] appear much smaller than those due to truncation errors of the finite-difference approximations. For a sufficiently small Δt, the difference between the explicit and implicit $\Delta(9,10)$ model formulations are small. Surprisingly, it is the implicit model that is computationally more efficient (see Table 3), which is most likely due to the better conditioning of the elliptic pressure operator in the implicit model formulation.

3.2 Idealized climates

The orographic planetary flow discussed in the preceding section, is fairly laminar and deterministic. The relevant results generated with many different variants of the model closely match each other, documenting both the hydrodynamic stability of the flow and robustness of the model design. The example considered in this section is very different in nature. Simulations of the idealized climates of Held and Suarez (1994) bear striking resemblance to large-eddy simulations (LES) of convective boundary layers (Nieuwstadt et al.1992), where small differences in model setups can lead to totally different instantaneous flow realizations, and where different model designs can lead to quite divergent integral flow characteristics. In other words, these simulated flows are both turbulent and chaotic.

Figure 3 illustrates the overall complexity of the flow. It shows instantaneous vertical cross-sections in the equatorial plane and surface plots of the isentropes Θ and isolines of zonal velocity u, after 3 years of simulated flow. The results displayed typify the response of an initially stagnant and uniformly stratified fluid to the diabatic forcing attenuating Θ and $\mathbf{v}$ to, respectively, the prescribed equilibrium temperature $\Theta_{EQ}(|y|, r')$ and $\mathbf{v}|_{r'<z_i} = 0$ (here, z_i represents a height of the boundary layer) in a manner mimicking the long term thermal and frictional forcings in the Earth atmosphere (see section 2 in Held and Suarez 1994, for details). The corresponding forcing functions augment the governing equations of motion (1a)-(1d) with appropriate Rayleigh friction and Newtonian cooling/heating terms.

The original forcing functions of Held and Suarez are expressed in the normalized pressure coordinates $\sigma \equiv p/p_s$ (where p_s and p denote, respectively, the full thermodynamic pressures at the surface and in the atmosphere aloft), so their diabatic forcing may evolve in time. In the anelastic model, only gradients of the perturbation pressure are meaningful and the full thermodynamic pressure is, in essence, unavailable. In order to avoid cumbersome procedures attempting to recover the true σ coordinate in our anelastic model, we have simply assumed a standard atmosphere with the density scale of 7 km to evaluate the fixed forcing functions. The significance of such a simplification can be

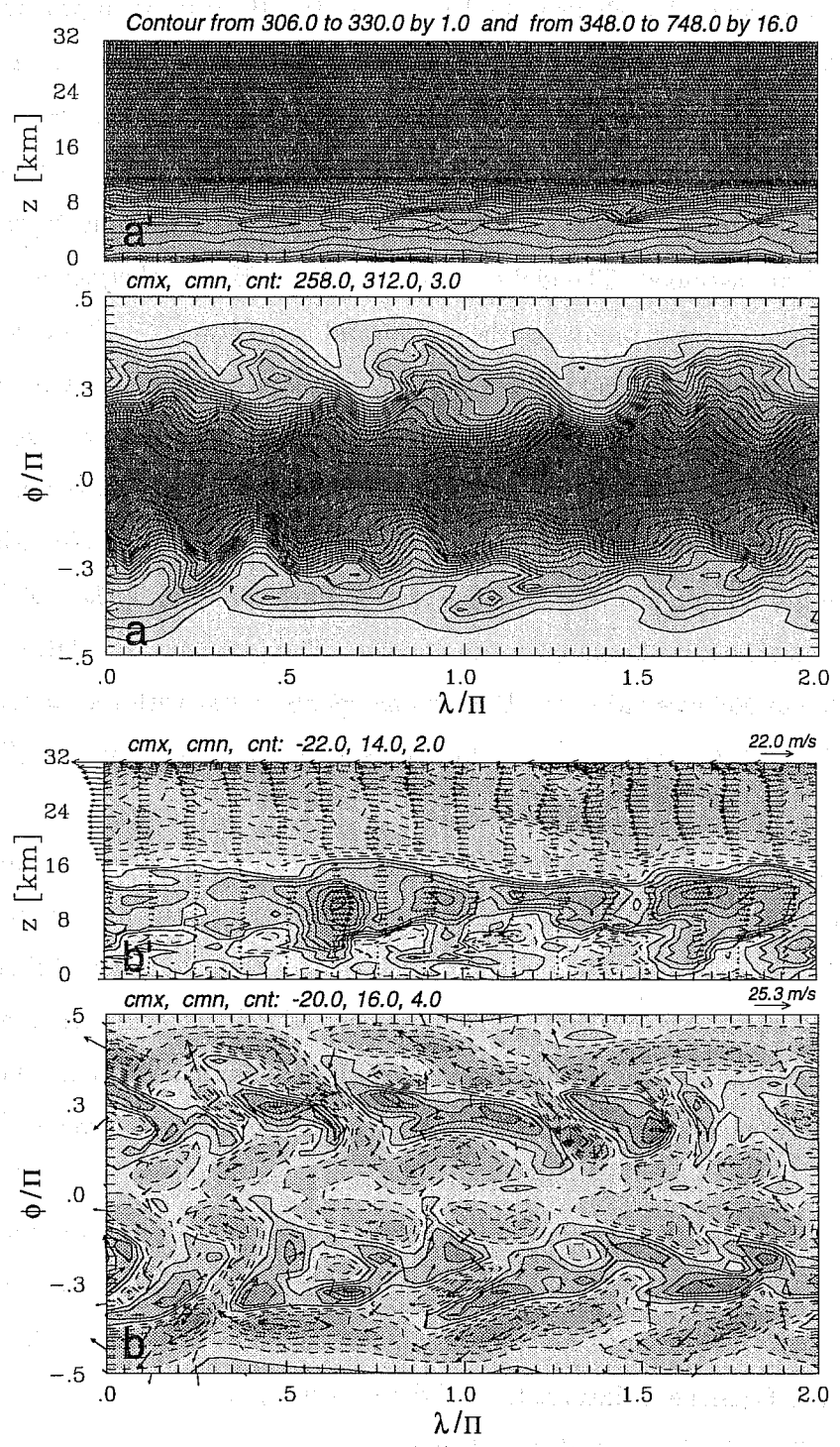

Figure 3: Instantaneous solutions of the idealized climate problem after 3 years of simulation. Plates a′ and *a* show Θ field in the vertical equatorial plane and at the surface, respectively. Plates b′ and b display the zonal velocity, respectively, in the equatorial plane and at the surface. Contour extrema and intervals are shown in the upper left corner of each plate (in plate a′ we used a variable contour to capture Θ variability in the troposphere). Negative values are dashed. Maximum vector lengths are shown in the upper right corner of plates b′ and b.

verified easily within the framework of a σ-coordinate model.

In section 3.1, we assumed a shallow fluid and used the Boussinesq approximation $\overline{\rho}(z_c) = \rho_o$ and $\overline{\Theta} = \Theta_o$. Here we consider a deep atmosphere and, therefore, solve the anelastic equations (1a)-(1e) with the variable reference density and potential temperature implied by $N = 10^{-2}$ s^{-1} Brunt-Väisällä frequency assumed for the reference state (cf. section 2b in Clark and Farley 1984). The implicit numerical model (section 2.2.4) is employed, and the environmental profiles $\mathbf{v}_e = 0$ and $\Theta_e = \Theta_{EQ}(\Pi/2,\ r')$ are assumed. The globe is covered with uniform spherical mesh with $nx \times ny = 64 \times 32$ grid intervals (no grid points at the poles) and the $H = 32 \cdot 10^3$ m deep atmosphere is resolved with $nz = 40$ uniform grid intervals. The time step of integration is $\Delta t = 900$ s. The dissipative filter in the polar regions assumes $\alpha = \tilde{\alpha}$ increasing linearly from 0 to $1/86400$ s^{-1} over the four grid intervals near each pole. Also, in lieu of the biharmonic diffusion used in the original Held-Suarez experiments, we exploit the implicit viscosity of the advection algorithms by employing the first-order upwind scheme at every 6th time step of the model (cf. Liska and Wendroff 1996) in both the Eulerian and the semi-Lagrangian simulations.[7] The particular simulation depicted in Fig. 3 used the massively parallel version[8] of the Eulerian model algorithm with the standard and linearized nonoscillatory MPDATA transport schemes for, respectively, Θ' and momenta (Smolarkiewicz and Margolin 1998).

Figure 4 contrasts the complexity of the instantaneous flow in Fig. 3 with the display of the resulting "climate", i.e., zonally-averaged three-year means of u and Θ (with the data from the first 200 days excluded). This figure corresponds to the results in Figs. 1 and 2 of Held and Suarez (1994). [Note that their plots are in the σ-coordinate.] The agreement of the two solutions is merely qualitative, which is not necessarily surprising taking into account the substantial differences between the models employed. Our trade winds and equatorial easterlies aloft are somewhat weaker, but our subpolar easterlies are more pronounced. Our westerlies are about as strong but shifted somewhat toward the equator. Although the Held-Suarez original solutions are for the primitive equations, we do not believe (based on the results of the preceding section) that either hydrostaticity, compressibility, or simplified Coriolis and metric forces are responsible for the differences observed. Among "physical" factors, perhaps the Boussinesq linearization of the pressure gradient terms may be important, but even this seems unlikely in the light of the following results.

We have performed numerous experiments addressing the sensitivity of Held-Suarez climates to various aspects of the numerical model design. Among these, we have tested sensitivities to the initial and

[7]Our semi-Lagrangian remapping procedure is built on nonoscillatory advection transport schemes similar to those used in the Eulerian model; Smolarkiewicz and Pudykiewicz 1992, Smolarkiewicz and Grell 1992.

[8]The parallelization strategy adopted in the global model (a single program multiple data, SPMD, message-passing approach with an explicit 2D horizontal grid decomposition) closely follows that used in the small-scale anelastic model (Anderson and Smolarkiewicz 1997, Anderson et al.1997), a precursor of the present code.

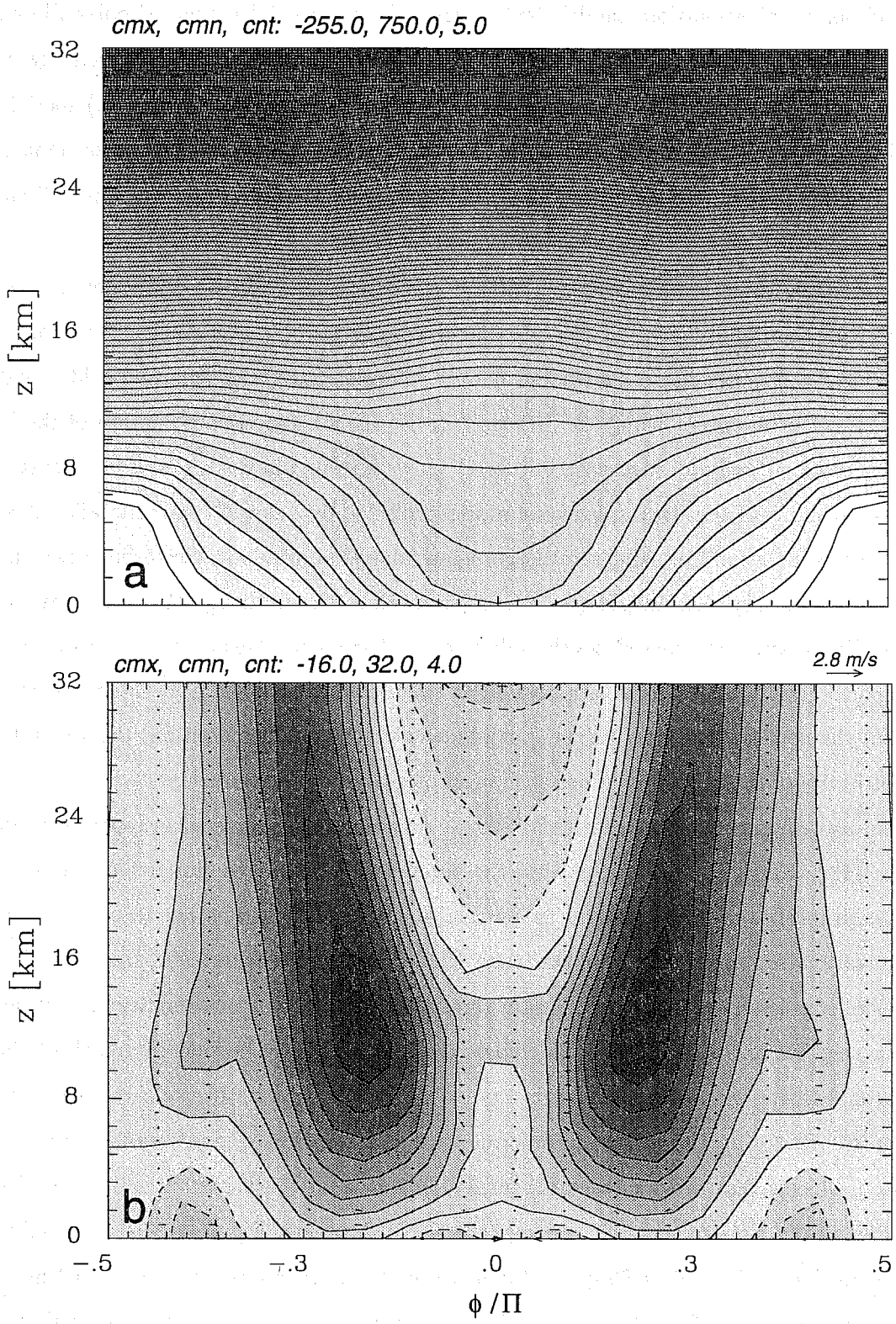

Figure 4: The zonally averaged 3-year means of potential temperature (plate a) and zonal velocity (plate b) for the simulation highlighted in Fig. 3. Contouring convention is similar to that used in Fig. 3.

ambient conditions, selected reference state, definition of the σ-coordinate in the forcing functions, spatial and temporal resolution, model depth, strength and spatial extent of polar filters, various viscosities in the model (in particular, the relative viscosity in the entropy and velocity equations, i.e., Prandtl number), flux versus advective (i.e., Eulerian versus semi-Lagrangian) model formulation, and linear z versus mass σ (recall $\delta p \sim \rho \delta z$) vertical coordinate representation (the latter has been achieved by an exponential stretching of the vertical coordinate mimicking σ coordinate for the standard atmosphere with the density scale height of 7 km).

We have found that the tropospheric climate is fairly robust (with details depending both on the model resolution and characteristics of polar filters), while the stratospheric solutions are quite sensitive even to fine details of the model design. For instance, the simulation identical to that summarized in Fig. 4, except using the linearized (a somewhat less viscous) option of the MPDATA advection scheme not only for momenta but for Θ' as well, results in weaker equatorial easterlies aloft and reduced stability of the stratospheric solution manifested by a slow $\mathcal{O}$(year) meridional oscillation. Also, a similar simulation but using semi-Lagrangian advection, produces westerlies whose magnitude increases monotonically with height (no closed jets). However, both models tend to reproduce the solution in Fig. 4 when the model depth is doubled and stretched "mass" coordinates are employed with a vertical gravity-wave absorber activated at the top of the model. Experiments with enhanced viscosity in the vertical transport terms (a crude convection parameterization) demonstrate another strong sensitivity of the solutions. More such examples could be presented.

The picture emerging from our sensitivity study—consistent with some other reported results (Chen and Bates 1996, Untch et al.1998)—is that the simulated Held-Suarez climates strongly depend on the viscous properties of the numerical models employed, regardless whether those come via explicit parameterizations or implicit effects of the truncation errors. In our experience, the lesser the viscosity of the model, the less robust are the climate simulations. The latter may appear discouraging as it suggests a need for an LES approach to climate modeling—clearly beyond the reach of the present computational technology. However, this is a point where nonhydrostatic global models may turn out to be helpful. Restoring less constrained forms of the Navier-Stokes' equations allows rescalings of the global problems that are unattainable in models based on the primitive equations. This opens new possibilities in climate research and modeling. To illustrate, Fig. 5 compares zonally-averaged instantaneous zonal winds after 90 days of simulation[9] on four abstract planets (starting in plate a with an Earth-like planet from Figs. 3 and 4) whose radius and temporal scales of diabatic forcings decrease by factor of 10 while the planetary rotation increases at the same rate to keep the Rossby number fixed. Thus, the planet in plate d, has a radius 6371.22 m and one day lasts there 86.4 s. The

[9]In our experience, zonal averages after about 2 months of simulation already give an adequate sense of the long-term mean climates.

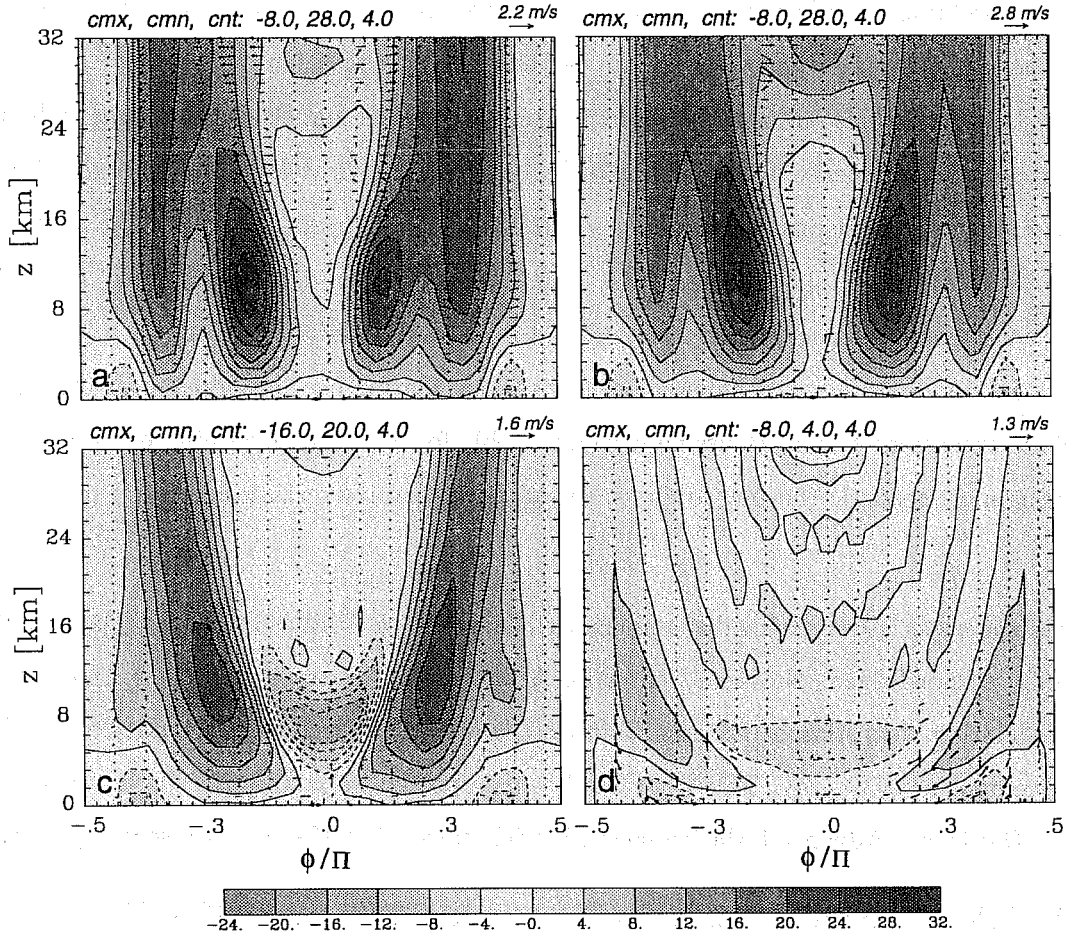

Figure 5: The zonally averaged instantaneous zonal velocity after 3 months of idealized climate simulations on rescaled planets with Rossby number kept constant. The Earth-like solution (corresponding to that in Fig. 4) is shown in plate a. Plates b, c, and d display the solutions for planets with the radius 10, 100, and 1000 times smaller, respectively. The contouring convention is the same as in Fig. 4.

results for the 10 and 100 times smaller planets already capture some of the characteristic features of the Earth climate. Thus, such rescaled globes could be employed to investigate effect of certain small- and mesoscale phenomena (e.g., gravity wave breaking, moist convection) on global flows and *vice versa*.

4. SUMMARY REMARKS

In the global atmospheric/oceanic modeling community, there is an apparent trend toward replacing the traditional hydrostatic primitive equations with less constrained nonhydrostatic forms of the Navier-Stokes' equations (Semmazi et al.1995, Marshall et al.1997, Cullen et al.1997). The few existing nonhydrostatic global models differ in analytic formulation and numerical design, reflecting their different purposes and origins.

We have extended our Cartesian NFT small-to-mesoscale model (broadly documented in the liter-

ature) to a mountaineous sphere and, consequently, have dispensed with the traditional geophysical simplifications of hydrostaticity, gentle terrain slopes, and weak rotation.

The results so far are encouraging: i) our nonhydrostatic global models preserve flow hydrostaticity; ii) their computational expense is comparable to that of present hydrostatic models, and can be greatly reduced by further acceleration of elliptic solvers. In light of these results, pursuit of the nonhydrostatic global approach seems well justified—at least in research models—especially in that nonhydrostatic models are more general, conceptually simpler, and more well posed.

The present model offers a number of opportunities for further development. Our immediate plans include extensions to non-Boussinesq compressible forms of the governing equations as well as incorporating more realistic thermal forcings, subgrid-scale parameterizations, moist processes, etc.

Acknowledgements. Stimulating discussions with James Hack, Philip Rasch, and David Williamson are gratefully acknowledged. National Center for Atmospheric Research is sponsored by the National Science Foundation. Los Alamos National Laboratory is operated by the University of California for the U.S. Department of Energy. This work has been supported in part by the Department of Energy "Computer Hardware, Advanced Mathematics, Model Physics" (CHAMMP) research program.

APPENDIX A GENERALIZED CONJUGATE-RESIDUAL APPROACH

Here we describe the preconditioned GCR(k) algorithm used in this study, special cases of which are discussed extensively in section 3 of Smolarkiewicz and Margolin (1994, hereafter SM94). We assume a general linear elliptic equation

$$\mathcal{L}(\phi) \equiv \sum_{I=1}^{M} \frac{\partial}{\partial x^I} \left(\sum_{J=1}^{M} C^{IJ} \frac{\partial \phi}{\partial x^J} + D^I \phi \right) - A\phi = R \,, \tag{A1}$$

with variable coefficients A, C^{IJ}, D^I, R, and either periodic, Dirichlet, or Neumann boundary conditions; and adopt the following notation. The discrete representation of a field on the grid is denoted by the subscript $\mathbf{i}$; the discrete representation of the elliptic operator on the lhs of (A1) is denoted by $\mathcal{L}_{\mathbf{i}}(\phi)$; and the inner product $\langle \xi \zeta \rangle \equiv \sum_{\mathbf{i}} \xi_{\mathbf{i}} \zeta_{\mathbf{i}}$. The preconditioner $\mathcal{P}$ is a linear operator that approximates $\mathcal{L}$ to a greater or lesser degree and $\mathcal{L}\mathcal{P}^{-1}$ is definite[10].

The GCR(k) method of Eisenstat et al.(1983) may be derived *via* the same variational arguments as those adopted in SM94 for the CR2 scheme—i.e., GCR(1) with $\mathcal{P} \equiv \mathcal{I}$, where $\mathcal{I}$ is the identity operator. Starting with a kth-order damped oscillation equation

$$\frac{\partial^k \mathcal{P}(\phi)}{\partial \tau^k} + \frac{1}{T_{k-1}(\tau)} \frac{\partial^{k-1} \mathcal{P}(\phi)}{\partial \tau^{k-1}} + \ldots + \frac{1}{T_1(\tau)} \frac{\partial \mathcal{P}(\phi)}{\partial \tau} = \mathcal{L}(\phi) - R \tag{A2}$$

[10]An operator $\mathcal{A}$ is said to be definite if $\langle \xi \mathcal{A}(\xi) \rangle$ is either strictly positive (positive definite) or strictly negative (negative definite) for all ξ.

in lieu of Eq. (2) in SM94, and proceeding with the formalism of sections 2 and 3 therein[11] leads to the following algorithm.

For any initial guess $\phi_{\mathbf{i}}^0$, set $r_{\mathbf{i}}^0 = \mathcal{L}_{\mathbf{i}}(\phi^0) - R_{\mathbf{i}}$, $p_{\mathbf{i}}^0 = \mathcal{P}_{\mathbf{i}}^{-1}(r^0)$; then iterate:

For $n = 1, 2, ...$until convergence do

for $\nu = 0, .., k-1$ do

$$\beta = -\frac{\langle r^\nu \mathcal{L}(p^\nu)\rangle}{\langle \mathcal{L}(p^\nu)\mathcal{L}(p^\nu)\rangle} , \tag{A3a}$$

$$\phi_{\mathbf{i}}^{\nu+1} = \phi_{\mathbf{i}}^\nu + \beta p_{\mathbf{i}}^\nu , \tag{A3b}$$

$$r_{\mathbf{i}}^{\nu+1} = r_{\mathbf{i}}^\nu + \beta \mathcal{L}_{\mathbf{i}}(p^\nu) , \tag{A3c}$$

$$\text{exit if } \| r^{\nu+1} \| \leq \varepsilon , \tag{A3d}$$

$$q_{\mathbf{i}} = \mathcal{P}_{\mathbf{i}}^{-1}(r^{\nu+1}) , \tag{A3e}$$

$$\mathcal{L}_{\mathbf{i}}(q) = \left[\sum_{I=1}^{M} \frac{\partial}{\partial x^I}\left(\sum_{J=1}^{M} C^{IJ}\frac{\partial q}{\partial x^J} + D^I q\right) - Aq\right]_{\mathbf{i}} , \tag{A3f}$$

$$\forall_{l=0,\nu} \quad \alpha_l = -\frac{\langle \mathcal{L}(q)\mathcal{L}(p^l)\rangle}{\langle \mathcal{L}(p^l)\mathcal{L}(p^l)\rangle} , \tag{A3g}$$

$$p_{\mathbf{i}}^{\nu+1} = q_{\mathbf{i}} + \sum_{l=0}^{\nu} \alpha_l p_{\mathbf{i}}^l , \tag{A3h}$$

$$\mathcal{L}_{\mathbf{i}}(p^{\nu+1}) = \mathcal{L}_{\mathbf{i}}(q) + \sum_{l=0}^{\nu} \alpha_l \mathcal{L}_{\mathbf{i}}(p^l) , \tag{A3i}$$

end do ,

$$\text{reset } [\phi,\ r,\ p,\ \mathcal{L}(p)]_{\mathbf{i}}^k \text{ to } [\phi,\ r,\ p,\ \mathcal{L}(p)]_{\mathbf{i}}^0 , \tag{A3j}$$

end do .

The GCR(k) scheme in (A3a)-(A3j) assumes a negative definite but not necessarily self-adjoint operator $\mathcal{L}$.[12] Direct evaluation of the elliptic operator on the grid takes place only once per iteration in (A3f).

[11] In essence, we discretize the oscillation equation in a pseudo-time τ, form the affine discrete equation for the progression of the residual errors r, and determine the optimal parameters $T_1, .., T_{k-1}$ and integration increment $\Delta\tau$ (variable in τ) that assure minimization of the residual errors in the norm defined by the inner product $\langle rr\rangle$.

[12] An operator $\mathcal{A}$ is said to be self-adjoint if $\langle \xi \mathcal{A}(\zeta)\rangle = \langle \zeta \mathcal{A}(\xi)\rangle$ for all ξ and ζ.

$$+(G^{13}\mathcal{F}_3 + G^{23})\vartheta_z\Big] \ , \tag{B7h}$$

$$\begin{aligned} C^{33} \;=\; & R\Big[(G^{13})^2 + (G^{23})^2(1+\mathcal{F}_2^2) + (G_0^{-1})^2(1+\mathcal{F}_3^2) + 2G_0^{-1}G^{23}\mathcal{F}_2\mathcal{F}_3\Big] + \\ & (1+\alpha^*)^{-1}\mathcal{G}\Big[-\Big((G^{23})^2\mathcal{F}_2 + G_0^{-1}G^{13} + G_0^{-1}G^{23}\mathcal{F}_3\Big)\vartheta_x \\ & + \Big(G^{13}G^{23}\mathcal{F}_2 + G_0^{-1}G^{13}\mathcal{F}_3 - G_0^{-1}G^{23}\Big)\vartheta_y \\ & + \Big((G^{13})^2 + (G^{23})^2\Big)\vartheta_z\Big] \ . \end{aligned} \tag{B7i}$$

For $\vartheta_x = \vartheta_y = \vartheta_z = 0$, the above expressions simplify to those of the explicit model (section 2.2.1).

REFERENCES

Anderson, W. D., and P. K. Smolarkiewicz, 1997: A comparison of high performance Fortran and message passing parallelization of a geophysical fluid model, in *Parallel Computational Fluid Dynamics: Algorithms and Results Using Advanced Computers*, Eds., P. Shiano, A. Ecer, J. Periaux, and N. Satofuka, Elsevier Science, 384–391.

Anderson, W. D., V. Grubišić, and P. K. Smolarkiewicz, 1997: Performance of a massively parallel 3D non-hydrostatic atmospheric fluid model. In *Proceedings of the International Conference on Parallel and Distributed Processing Techniques and Applications*, PDPTA'97, Las Vegas, Nevada, USA, June 30-July 3, Ed. H. R. Arabnia, CSREA, 645–651.

Chen, M., and J. R. Bates, 1996: A comparison of climate simulations from a semi-Lagrangian and an Eulerian GCM. *J. Climate*, **9**, 1126–1149.

Chorin, A. J., 1968: Numerical solution of the Navier-Stokes equations. *Math. Comp.*, **22**, 742–762.

Clark, T. L., 1977: A small-scale dynamic model using a terrain-following coordinate transformation. *J. Comput. Phys.*, **24**, 186–214.

Clark, T. L., and R. D. Farley, 1984: Severe downslope windstorm calculations in two and three spatial dimensions using anelastic interactive grid nesting: A possible mechanism for gustiness. *J. Atmos. Sci.*, **41**, 329–350.

Clark, T. L., W. D. Hall, and J. L. Coen, 1996: Source code documentation for the Clark-Hall cloud-scale model code version G3CH01. National Center for Atmospheric Research, Technical Note No. NCAR/TN-426+STR, 175 pp.

Cullen, M. J. P., T. Davies, M. H. Mawson, J. A. James, and S. Coulter, 1997: An overview of numerical methods for the next generation UK NWP and climate model, *Atmosphere-Ocean Special*, **35**, 425–444.

Eisenstat, S. C., H. C. Elman, and M. H. Schultz, 1983: Variational iterative methods for nonsymmetric systems of linear equations. *SIAM J. Numer. Anal.*, **20**, 345–357.

Gal-Chen, T., and R. C. J. Somerville, 1975: On the use of a coordinate transformation for the solutions of the Navier-Stokes equations. *J. Comput. Phys.*, **17**, 209–228.

Gill, A. E., 1982: *Atmosphere-Ocean Dynamics*. Academic Press, 662 pp.

Grose, W. L., and B. J. Hoskins, 1979: On the influence of orography on large-scale atmospheric flow. *J. Atmos. Sci.*, **36**, 223–234.

Held, I. M., and M. J. Suarez, 1994: A proposal for intercomparison of the dynamical cores of atmospheric general circulation models, *Bull. Amer. Meteor. Soc.*, **75**, 1825–1830.

Kapitza, H., and D. Eppel, 1992: The non-hydrostatic mesoscale model GESIMA. Part 1: Dynamical equations and tests. *Beitr. Phys. Atmosph.*, **65**, 129–146.

Liska, R., and B. Wendroff, 1996: Composite schemes for conservation laws. Technical Report LA-UR 96-3589, LANL, Los Alamos, 20 pp. SIAM J. Numer. Anal., 1997, to appear.

Marshall, J., A. Adcroft, C. Hill, L. Perelman, and C. Heisey, 1997: A finite-volume incompressible Navier Stokes model for studies of the ocean on parallel computers. *J. Geophys. Res.*, **102**(C3), 5753–5766.

Marshall, J., C. Hill, L. Perelman, and A. Adcroft, 1997: Hydrostatic, quasi-hydrostatic, and non-hydrostatic ocean modeling. *J. Geophys. Res.*, **102**(C3), 5733–5752.

Nieuwstadt, F. T. M., P. J. Mason, C-H Moeng, and U. Schumann, 1992: Large-eddy simulation of convective boundary-layer: A comparison of four computer codes, *Turbulent Shear Flows 8*, H. Durst et al., Eds., Springer-Verlag, 343–367.

Roache, P., J., 1972: *Computational Fluid Dynamics.*, Hermosa Publishers, Albuquerque, 446 pp.

Rotunno, R., and P. K. Smolarkiewicz, 1995: Vorticity generation in the shallow-water equations as applied to hydraulic jumps. *J. Atmos. Sci.*, **52**, 320–330.

Semazzi, F. H. M., J.-H. Qian, and J. S. Scroggs, 1995: A global nonhydrostatic semi-Lagrangian, atmospheric model without orography. *Mon. Wea. Rev.*, **123**, 2534–2550.

Skamarock, W. C., P. K. Smolarkiewicz, and J. B. Klemp, 1997: Preconditioned conjugate-residual solvers for Helmholtz equations in nonhydrostatic models. *Mon. Wea. Rev.*, **125**, 587–599.

Smolarkiewicz, P. K., and T. L. Clark, 1986: The multidimensional positive definite advection transport algorithm: Further development and applications, *J. Comput. Phys.*, **67**, 396–438.

Smolarkiewicz, P. K., and G. A. Grell, 1992: A class of monotone interpolation schemes, *J. Comput. Phys.*, **101**, 431–440.

Smolarkiewicz, P. K., and J. A. Pudykiewicz, 1992: A class of semi-Lagrangian approximations for fluids. *J. Atmos. Sci.*, **49**, 2082–2096.

Smolarkiewicz, P. K., and L. G. Margolin, 1993: On forward-in-time differencing for fluids: Extension to a curvilinear framework, *Mon. Wea. Rev.*, **121**, 1847–1859.

Smolarkiewicz, P. K., and L. G. Margolin, 1994: Variational solver for elliptic problems in atmospheric flows, *Appl. Math. & Comp. Sci.*, **4**, 527–551.

Smolarkiewicz, P. K., and L. G. Margolin, 1997: On forward-in-time differencing for fluids: An Eulerian/semi-Lagrangian nonhydrostatic model for stratified flows. *Atmos. Ocean Special*, **35**, 127–152.

Smolarkiewicz, P. K., V. Grubišić, and L. G. Margolin, 1997: On forward-in-time differencing for fluids: Stopping criteria for iterative solutions of anelastic pressure equations, *Mon. Wea. Rev.*, **125**, 647–654.

Smolarkiewicz, P. K., and L. G. Margolin, 1998: MPDATA: A finite-difference solver for geophysical flows, *J. Comput. Phys.*, **140**, 459-480.

Untch, A., Ch. Jablonowski, and M. Hortal, 1998: Results of dynamical core tests at ECMWF. 6^{th} *Workshop on Numerical Solutions of Fluid Flow in Spherical Geometry*, Gatlinburg, Tennessee, April 28 - May 1.

Williamson, D. L., J. B. Drake, J. J. Hack, R. Jakob, and P. N. Swarztrauber, 1992: A standard test set for numerical approximations to the shallow water equations on the sphere, *J. Comput. Phys.*, **102**, 211–224.